Valley polarization braiding in strained graphene

D. Faria [1,2] C. León,[3] L. R. F. Lima [3,4] A. Latgé [3] and N. Sandler [2]

[1]*Instituto Politécnico, Universidade do Estado do Rio de Janeiro, Nova Friburgo, Rio de Janeiro 28625-570, Brazil*
[2]*Department of Physics and Astronomy, Ohio University, Athens, Ohio 45701-2979, USA*
[3]*Instituto de Física, Universidade Federal Fluminense, Niterói, Rio de Janeiro 24210-340, Brazil*
[4]*Departamento de Física, Universidade Federal Rural do Rio de Janeiro, Seropédica, Rio de Janeiro 23897-000, Brazil*

Previous works on deformed graphene predict the existence of valley-polarized states, however, optimal conditions for their detection remain challenging. We show that in the quantum Hall regime, edgelike states in strained regions can be isolated in energy within Landau gaps. We identify precise conditions for conducting edgelike states to be valley polarized. By the appropriate design of strain profiles these states can be positioned at chosen locations in the sample. A map of the local density of states as a function of energy and position reveals a unique braid pattern that serves as a fingerprint to identify valley polarization.

Strained graphene has emerged as an important tool to implement valleytronic-based devices [1–14] and, in particular, in protocols for quantum computation [15]. Recent experimental developments show that substrate engineering can be used to design deformation geometries with specific strain profiles [16–34]. Clear signatures of valley splitting in confined geometries represent an important step in this direction, as exemplified by scanning tunneling microscope (STM) studies on graphene quantum dots [35,36]. In extended configurations, similar observations have been reported on multiple fold structures [28,29] with preliminary evidence of valley-polarized states. These studies are supported by previous work that predicted strained regions to act as waveguides for electron currents [6–10]. However, several drawbacks still exist because the optimal conditions for the creation and detection of valley-split currents are not well defined.

To take advantage of the existence of valley-polarized channels, it is crucial to separate their contribution from graphene's conducting background. This can be achieved by introducing an external magnetic field large enough to take the system into the quantum Hall (QH) regime [37–49]. As we show below, strained regions in the QH regime allow (1) the generation of valley-polarized edgelike states with energies inside the Landau gaps, and (2) the freedom to position them anywhere in the sample by the proper design of strain fields. This feature adds the flexibility to accommodate contact probes to collect individual valley currents.

STM measurements of the local density of states (LDOS) in strained graphene areas exhibit characteristic split peaks that reflect the breaking of Landau level (LL) degeneracies, although not necessarily valley polarization. We address this issue by calculating the LDOS of graphene with a foldlike deformation that describes the evolution of peak splittings and the emergence of a regime with valley polarization. Furthermore, as the deformed region is traversed, maximum LDOS intensities for each valley evolve in energy, leading to a braid structure that serves as a unique fingerprint of

valley-polarized states. Under bias, these states generate extra conducting channels that can be visualized as edge states along the strained region.

In order to bring attention to the interplay between deformation parameters and magnetic length, we perform combined analytical and numerical studies based on the continuum and tight-binding descriptions of electrons in graphene. As we are interested in the QH regime, the deformation is included as a perturbation for LL levels. Our results show the existence of two distinct regimes characterized by $\gamma = l_B/b$, i.e., the ratio between the magnetic length l_B and the deformation width b. For $\gamma > 1$ the broad LL states average over the deformed region. In contrast, for $\gamma < 1$ the magnetic confinement allows the electrons to follow the inhomogeneous strain profile. In this last regime, the spatial separation between the polarized states becomes larger, an attractive feature for quantum device design [15], as it improves the detection of polarized currents.

Model. The electronic properties of strained graphene in the presence of a magnetic field are described by the nearest-neighbor tight-binding Hamiltonian [50]

$$H = \sum_{\langle i,j \rangle} t_{ij} c_i^\dagger c_j + \text{H.c.}, \tag{1}$$

where $c_i^\dagger$ (c_i) is the creation (annihilation) field operator in the ith site. The modified nearest-neighbor hopping energy t_{ij} is given by [39,50–53]

$$t_{ij} = t_0 e^{i\Delta\phi_{i,j}} e^{-\beta(\frac{l_{ij}}{a_{cc}}-1)}, \tag{2}$$

where $\beta = |\partial \log t_0 / \partial \log a_{cc}| \approx 3$, t_0 is the hopping parameter of pristine graphene, and a_{cc} is its lattice parameter. The magnetic field is included via the Peierls substitution, $\Delta\phi_{i,j} = 2\pi(e/h) \int_{\mathbf{r}_j}^{\mathbf{r}_i} \mathbf{A} \cdot d\mathbf{r}$, with $\mathbf{r}_i$ and $\mathbf{r}_j$ being the nearest-neighbor positions. The strain field, given in terms of the elasticity tensor ε, modifies interatomic distances $l_{ij} = \frac{1}{a_{cc}}(a_{cc}^2 + \varepsilon_{xx}x_{ij}^2 + \varepsilon_{yy}y_{ij}^2 + 2\varepsilon_{xy}x_{ij}y_{ij})$, where x_{ij} and y_{ij}
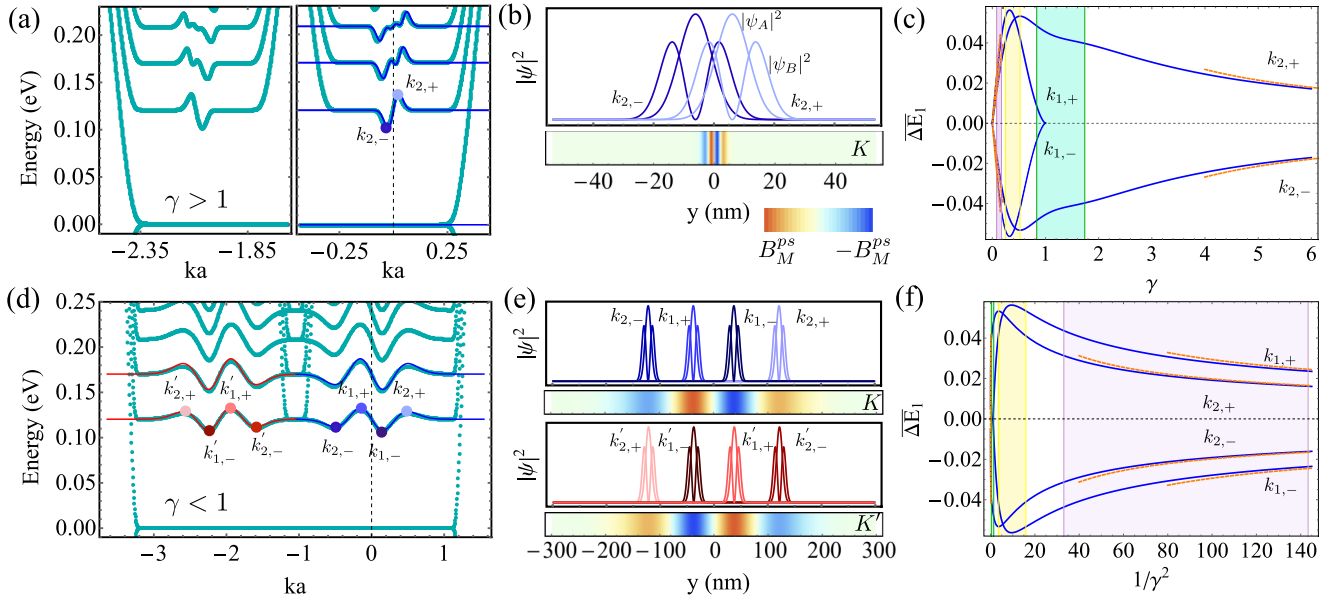
FIG. 1. (a) and (d) Comparison between continuum [blue (K) and red (K')] and tight-binding (cyan) band structure results for deformed graphene in the QH regime. (b) and (e) Probability density distributions for k states identified in (a) and (d). Bottom: Contour plot of pseudomagnetic field with maximum values of (b) $B_M^{ps} = 82$ T and (e) $B_M^{ps} = 2.3$ T. Parameters: (a) and (b) $\gamma = 2.7$, $b = 20a_{cc}$, $\xi = 0.2$, maximum strain $\varepsilon_M = 1.5\%$, and (d) and (e) $\gamma = 0.07$, $b = 800a_{cc}$, $\xi = 0.22$, $\varepsilon_M = 1.7\%$. $B = 11$ T for both cases. (c) and (f) Scaling of the first LL energy correction ΔE_1 in units of ($\xi^2 t'$), as a function of γ and $1/\gamma^2 \propto B$, respectively. Continuum (blue) lines represent the exact evaluation of energy corrections while dashed (orange) lines correspond to analytic expressions in the asymptotic regimes given by Eq. (9).

correspond to the projected distance between sites i and j before the deformation. In these expressions the x axis is chosen along the zigzag direction. At low energies the effective continuum Hamiltonian is given by two copies of a two-dimensional (2D) Dirac equation $H_{K(K')}^D = v_F \boldsymbol{\sigma} \cdot \mathbf{p}$ written in the valley-symmetric representation. Here, $v_F \approx 10^6$ m/s is the Fermi velocity [54], $\boldsymbol{\sigma} = (\sigma_x, \sigma_y)$ are Pauli matrices acting on the pseudospin degree of freedom associated with the sublattice (A, B) structure of the honeycomb lattice, and $\mathbf{p}$ is the electronic momentum around the K (K') point. The magnetic field is implemented using the minimal coupling $\mathbf{p} = \mathbf{p} + e\mathbf{A}$ in the Landau gauge, as $\mathbf{A} = B(-y, 0)$. The unstrained system has relativistic LLs given by $E_N = \pm \frac{\hbar v_F}{l_B} \sqrt{2N}$, with the $\pm$ representing conduction and valence bands, respectively. The magnetic length is given by $l_B = \sqrt{\frac{\hbar}{eB}}$, and N is the integer label for the Nth LL.

To study the effects of strain in this regime we chose to represent a nonuniform strain field with a model for a foldlike deformation with a height profile,

$$h(y) = h_0 e^{-\frac{(y-y_0)^2}{b^2}}, \qquad (3)$$

where h_0 and b describe the amplitude and width of the fold, respectively, and y_0 indicates the position of its center. In the continuum limit, the corresponding strain tensor $\epsilon_{ij} = \frac{1}{2}\partial_i h \partial_j h$ gives rise to the pseudogauge field [55]

$$\begin{pmatrix} A_x^{ps} \\ A_y^{ps} \end{pmatrix} = \begin{pmatrix} \varepsilon_{xx} - \varepsilon_{yy} \\ -2\varepsilon_{xy} \end{pmatrix} = \begin{pmatrix} -2\frac{y^2}{b^4}h(y)^2 \\ 0 \end{pmatrix}, \qquad (4)$$

and a pseudomagnetic field $\mathbf{B}_{K(K')}^{ps} = \pm \frac{\Phi_0}{(2\pi)} \left(\frac{-\beta}{2a_{cc}}\right) \boldsymbol{\nabla} \times \mathbf{A}^{ps}$, with $+ (-)$ for valley K (K'), where Φ_0 is the unit of quantum

flux. The model, chosen to emphasize the spatial dependence of $\mathbf{B}^{ps}$ [contour plots at the bottom of Figs. 1(b) and 1(e)], reveals physical features that are determined by the extension of the deformed region b. These features should be observable in samples with more general nonuniform strain profiles, thus making our predictions relevant for a broad range of experimental setups. In addition to $\mathbf{A}^{ps}$, strain introduces an effective scalar field [55–59] that is less important for the valley-polarized regime as discussed in the Supplemental Material (SM) [60].

The electron dynamics is governed by [41,43,50,51]

$$H_{K(K')} = \hbar v_F \boldsymbol{\sigma} \cdot \left(-i\boldsymbol{\nabla} - \frac{e}{\hbar}\mathbf{A} \pm \frac{\beta}{2a_{cc}}\mathbf{A}^{ps}\right). \qquad (5)$$

Since we are interested in the QH regime, $\mathbf{A}^{ps}$ due to the deformation is treated as a perturbation. Because of the x-direction translation invariance, Eq. (5) allows solutions of the form $\Psi(x, y) = \psi(y)e^{ikx}$. The effective one-dimensional Hamiltonian reduces to

$$\begin{pmatrix} 0 & \hat{\mathcal{O}} \mp t'(\xi\gamma)^2\varepsilon_{\tilde{y}\tilde{y}} \\ \hat{\mathcal{O}}^+ \mp t'(\xi\gamma)^2\varepsilon_{\tilde{y}\tilde{y}} & 0 \end{pmatrix}\psi(\tilde{y}) = E\psi(\tilde{y}), \quad (6)$$

with $\hat{\mathcal{O}} = \frac{\hbar\omega_c}{\sqrt{2}}(\partial_{\tilde{y}} + \tilde{y})$, $\hat{\mathcal{O}}^+ = \frac{\hbar\omega_c}{\sqrt{2}}(-\partial_{\tilde{y}} + \tilde{y})$, and $\omega_c = \frac{\sqrt{2}v_F}{l_B}$. Dimensionless coordinates are defined as $\tilde{x} = x/l_B$, $\tilde{y} = (y/l_B - \tilde{k})$, $\tilde{k} = kl_B$, and $t' = \beta\hbar v_F/a_{cc} \approx 13.9$ eV is the effective hopping. The deformation parameter $\xi = (h_0/b)$ characterizes the strain intensity $\varepsilon_M = \xi^2/e$ (e = Euler number), and $\varepsilon_{\tilde{y}\tilde{y}} = (\tilde{y} + \tilde{k})^2 e^{-2(\tilde{y}+\tilde{k})^2\gamma^2}$ is the dimensionless strain tensor.

The analysis of the continuum model is done with perturbation theory techniques for energy and eigenstates with

unperturbed spinor eigenstates given by

$$\Psi^0(\tilde{x}, \tilde{y}) = \frac{1}{\sqrt{2}} \sqrt{\frac{l_B}{L_x}} \begin{pmatrix} \psi_{N-1}(\tilde{y}) \\ \pm \psi_N(\tilde{y}) \end{pmatrix} e^{i\tilde{k}\tilde{x}}, \quad (7)$$

where $\psi_N(\tilde{y}) = 2^{-N/2}(N!)^{-1/2} e^{-\tilde{y}^2/2} H_N(\tilde{y})$, $H_N(\tilde{y})$ is the Hermite polynomial of the Nth order, $L_x (\to \pm \infty)$ rises from the normalization of the plane wave, and $\pm$ corresponds to positive and negative energies, respectively.

The change in the energy of the Nth LL is

$$\Delta E_N(\tilde{k}) = -t'(\xi\gamma)^2 \int_{-\infty}^{\infty} \varepsilon_{\tilde{y}\tilde{y}}(\tilde{y}, \tilde{k}) \psi_{N-1}(\tilde{y}) \psi_N(\tilde{y}) d\tilde{y}. \quad (8)$$

The analytic solution of the integral provides an exact expression for the energy corrections and allows us to derive expressions for the reduced gaps at large and small values of γ (see Fig. 1 and SM [60]). The closing of gaps between consecutive LLs is the criteria used to establish convergence of the perturbation expansion. As discussed in SM [60], this condition implies $\varepsilon_M < \hbar\omega_c(\sqrt{N+1} - \sqrt{N})/(0.112t'e)$.

For a fixed strain value ($\xi = $ const), the first LL corrections are

$$\Delta E_1 = \pm c_1 t' \xi^2 \gamma^{-1} + O[\gamma^{-3}], \quad \text{for } \gamma \gg 1,$$
$$\Delta E_1 = \pm c_{2(3)} t' \xi^2 \gamma + O[\gamma^3], \quad \text{for } \gamma \ll 1. \quad (9)$$

with constant values $c_1 \approx 0.1$, $c_2 \approx 0.2$, and $c_3 \approx 0.3$. These expressions are confirmed by higher-order results (see SM [60]), as well as by numerical solutions for Eq. (1) implemented in a ribbon geometry with zigzag termination along the fold axis direction (the ribbon's widths were appropriately chosen to avoid edge effects). We show that, in contrast to previous works [2,29,39–41], valley-polarized currents can be generated even in perfect symmetric configurations and generic inhomogeneous strain fields in the appropriate regimes.

Results. Figure 1 shows a comparison between continuum and tight-binding results for fixed $B = 11$ T. Figures 1(a) and 1(d) show band structure results for $\gamma > 1$ and $\gamma < 1$, respectively, with parameters appropriate for currently available experimental realizations [25–34]. The general profile for both band structures shows modifications in the gaps between LLs. As expected, the pseudofield preserves electron-hole symmetry [61] and the zeroth LL is not affected. For a given level, the two regimes exhibit different numbers of local energy minima and maxima, indicated by $(k_{1,\pm}; k_{2,\pm})$ in the first LL for the K valley (results for K' are obtained by spatial inversion). The finer structure that develops at higher LLs is produced by the inhomogeneous nature of the strain field revealing a larger number of states affected at higher energies. Notice the excellent agreement between the analytic (blue solid line) and numerical (cyan dots) results in both regimes. In Figs. 1(b) and 1(e), probability densities are presented for the states color coded by the dots in Figs. 1(a) and 1(d), on top of the corresponding pseudomagnetic field contours. For $\gamma > 1$, as the confinement due to the external field is larger than the extent of the deformation, the electronic density is spread beyond the region of the pseudofield, while for $\gamma < 1$, the states are localized at four distinct regions following the
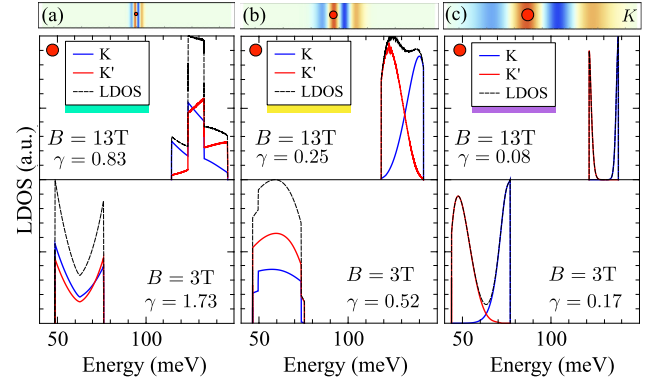

FIG. 2. LDOS for valleys K and K' (blue and red) for deformations (h_0, b): (a) $(9a_{cc}, 60a_{cc})$, (b) $(25a_{cc}, 200a_{cc})$, and (c) $(95a_{cc}, 600a_{cc})$, with different values of strain smaller than 1%, and external fields, $B = 13$ T (top panels) and 3 T (bottom). Pseudomagnetic field contour plots are shown on top of the corresponding LDOS. Results obtained for positions where the pseudofield is maximum, as depicted with the red circles.

pseudofield profile. These features are a manifestation of valley polarization in space.

Figures 1(c) and 1(f) depict the different scaling of maxima and minima energy corrections for the first LL, $\overline{\Delta E_1} = \Delta E_1/(\xi^2 t')$, obtained with Eq. (8) as a function of γ and $1/\gamma^2$, respectively (blue online). Data are presented for valley K (identical results for K'). The four energy corrections for states $(k_{1,\pm}, k_{2,\pm})$ identified in Fig. 1(d) are plotted. The dependence with γ in Fig. 1(c) shows the vanishing of the correction at $\gamma = 1$ for states labeled by $k_{1,\pm}$, signaling the change in regimes from $\gamma < 1$ to $\gamma > 1$. For $\gamma \gg 1$ the correction vanishes as expected because $\mathbf{B}^{ps}$ is concentrated in a narrower region compared to the LL confinement, even when $|\mathbf{B}^{ps}| \gg |B|$. The dependence for $\gamma < 1$ is better appreciated in Fig. 1(f), where $\overline{\Delta E_1}$ is plotted as a function of $1/\gamma^2$. Notice that the asymptotic behavior indicates vanishing of the corrections as the pseudofield decreases in magnitude while occupying a larger region of the sample. The spreading of $\mathbf{B}^{ps}$ in a larger area allows for a definite resolution of its sign alternation, leading to the spatial separation of the four states. The exact solution for all values of γ is compared with the analytic expression [Eq. (9)], shown with dashed lines (orange online), exhibiting excellent agreement in the two regimes. For $\gamma \ll 1$, the expression for the LL energies, $E_N + \Delta E_N \propto \sqrt{(B \pm B_M^{ps})}$, reproduces the expected scaling for an effective magnetic field [60]. The colored areas in Figs. 1(c) and 1(f) depict the transition between $\gamma \gg 1$ and $\gamma \ll 1$ regimes.

Calculation of LDOS to second order provides signatures of the transition that could be observed in STM measurements as shown in Fig. 2. Results for LDOS at valleys K and K' (blue and red online) are presented for values of γ at both boundaries of each colored shaded area in Figs. 1(c) and 1(f), corresponding to $B = 13$ and 3 T. The LDOS is plotted at positions marked by the red dot on the $\mathbf{B}^{ps}$ contour plots (presented for a fixed length to emphasize the different widths b used). Although some panels show peak splittings in the LDOS, not all splittings represent valley-polarized regimes. As Fig. 2(a) shows, there is a broadened LL peak for
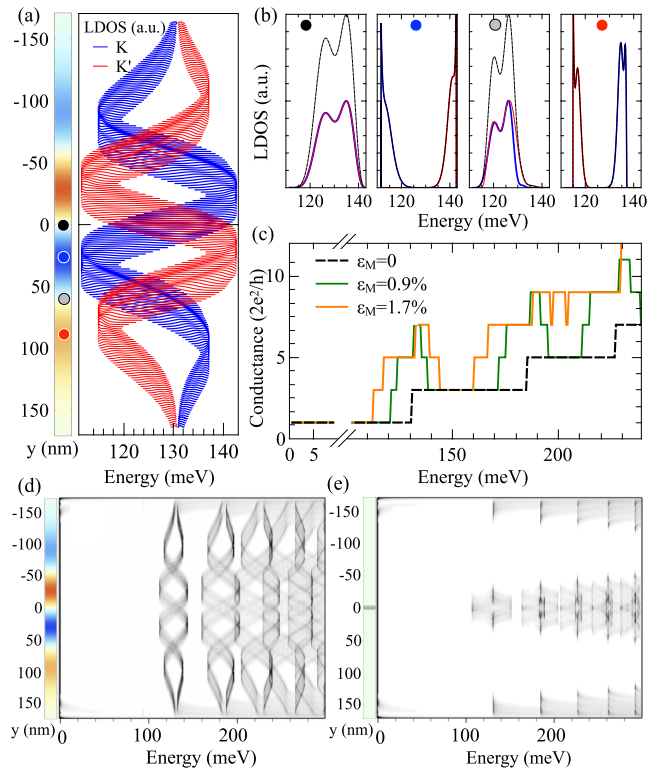
FIG. 3. (a) LDOS vs energy at different positions across the deformation (y direction) for valleys K and K' (blue and red). The pseudofield profile for valley K is displayed by the colored bar. (b) LDOS × energy for specific positions marked by colored dots in the pseudofield profile. Curves were enlarged from (a) for clarity. Black curves represent the LDOS with a contribution from both valleys. Parameters: $B = 13$ T, $b = 600a_{cc}$, $\varepsilon_M = 1.7\%$, and $\gamma = 0.08$. (c)–(e) Results obtained for a zigzag ribbon with $B = 13$ T. (c) Two-terminal conductance along the deformation. LDOS × energy at different positions across the deformation (d) $\gamma = 0.08$ and (e) $\gamma = 2.8$.

$B = 13$ T ($\gamma = 0.83$) and a split peak for $B = 3$ T ($\gamma = 1.73$), not valley polarized. In contrast, Fig. 2(b) shows broadened peaks for both fields ($\gamma = 0.52$ and $\gamma = 0.25$). As predicted, valley polarization is only clearly resolved for values $\gamma \ll 1$, as shown in Fig. 2(c) ($\gamma = 0.17$ and $\gamma = 0.08$). Valley-polarized peaks resemble van Hove singularities representing edge states emerging at the deformed region. In all cases, peak energies can be obtained from Eq. (8), and splittings could be engineered by an appropriate choice of the strain intensity for fixed γ.

To further investigate valley splittings, Fig. 3(a) shows LDOS versus energy curves for K and K' valleys (blue and red) at different positions across the deformation for $\gamma = 0.08$. As one moves from one side of the deformation to the other (y axis), the maxima LDOS intensities braid in a precise pattern that distinguish each valley contribution. The origin

of this peculiar pattern can be traced back to Fig. 1, where the energy difference between states from valleys K and K' is a consequence of different signs of $\mathbf{B}^{ps}_{K(K')}$. For example, at the position indicated by the blue dot ($y \simeq 25$ nm), the LDOS peak at low energy corresponds to valley K, while at the red dot position ($y \simeq 75$ nm), it corresponds to valley K'. As $\mathbf{B}^{ps}$ changes across the deformation, the magnitude of the splittings also changes, resulting in the braiding signature. Figure 3(b) shows LDOS with contributions from both valleys (black curves) and highlights the evolution of valley polarization for particular positions across the ribbon. Peak splittings are still observed at positions with $\mathbf{B}^{ps} = 0$ (black and gray dots), due to the finite extension of wave functions and the inhomogeneous $\mathbf{B}^{ps}$. Although all panels show a double-peak structure, only two of them correspond to valley-polarized states, emphasizing the relevance of the braiding structure to detect valley polarization. These states will appear in transport measurements as four conducting channels at the deformed region. Figure 3(c) compares conductance results, obtained with Green's function methods [62], for ribbons with different strain intensities. As expected, conductance plateaus appear at energies corresponding to van Hove singularities. An appropriate space separation between these channels can be adjusted by choosing b, thus enhancing the collection of separate valley currents. Furthermore, these channels are robust against edge disorder as the deformation resides inside the sample.

Finally, differences between regimes $\gamma > 1$ and $\gamma < 1$ are clearly identified in Figs. 3(d) and 3(e), where tight-binding results for LDOS peaks are presented. Figure 3(d) ($\gamma = 0.08$) shows braiding features visible in several Landau levels. At higher levels the gaps close and valley polarization vanishes. In Fig. 3(e) ($\gamma = 2.8$), it is still possible to distinguish peak splittings, however, the braiding pattern is absent. Valley polarization disappears for $\gamma > 1$.

Conclusions. In conclusion, deformed graphene in the QH regime provides a perfect playground to create valley-polarized conducting channels. These appear whenever the sample is set up in the regime $l_B/b \ll 1$, at energies within LL gaps and at chosen locations in the sample. The separation of valley-polarized states gives rise to a unique braid pattern that should be observable in STM measurements of LDOS as the deformation is crossed. Hence, extended deformed graphene configurations offer versatile setups to design electronic devices.

[1] Y. Jiang, T. Low, K. Chang, M. I. Katsnelson, and F. Guinea, Phys. Rev. Lett. **110**, 046601 (2013).

[2] M. Settnes, S. R. Power, M. Brandbyge, and A.-P. Jauho, Phys. Rev. Lett **117**, 276801 (2016).

[3] G. W. Jones, D. A. Bahamon, A. H. Castro Neto, and V. M. Pereira, Nano Lett. **17**, 5304 (2017).

[4] X.-P. Zhang, C. Huang, and M. A. Cazalilla, 2D Mater. **4**, 024007 (2017).

[5] T. Stegmann and N. Szpak, 2D Mater. **6**, 015024 (2018).

[6] D.-B. Zhang, G. Seifert, and K. Chang, Phys. Rev. Lett. **112**, 096805 (2014).

[7] P. Ghaemi, S. Gopalakrishnan, and S. Ryu, Phys. Rev. B **87**, 155422 (2013).

[8] V. Torres, D. Faria, and A. Latgé, Phys. Rev. B **97**, 165429 (2018).

[9] R. Carrillo-Bastos, C. Leon, D. Faria, A. Latgé, E. Y. Andrei, and N. Sandler, Phys. Rev. B **94**, 125422 (2016).

[10] D. Zhai and N. Sandler, Phys. Rev. B **98**, 165437 (2018).

[11] S. P. Milovanović and F. M. Peeters, J. Phys.: Condens. Matter **29**, 075601 (2016).

[12] V. O. Shubnyi and S. G. Sharapov, Low Temp. Phys. **43**, 1202 (2017).

[13] R. Carrillo-Bastos, M. Ochoa, S. A. Zavala, and F. Mireles, Phys. Rev. B **98**, 165436 (2018).

[14] M. M. Grujić, M. Z. Tadić, and F. M. Peeters, Phys. Rev. Lett. **113**, 046601 (2014).

[15] Y. S. Ang, S. A. Yang, C. Zhang, Z. Ma, and L. K. Ang, Phys. Rev. B **96**, 245410 (2017).

[16] J. S. Bunch, S. S. Verbridge, J. S. Alden, A. M. van der Zande, J. M. Parpia, H. G. Craighead, and P. L. McEuen, Nano Lett. **8**, 2458 (2008).

[17] N. Levy, S. A. Burke, K. L. Meaker, M. Panlasigui, A. Zettl, F. Guinea, A. H. Castro Neto, and M. F. Crommie, Science **329**, 544 (2010).

[18] N. Lindahl, D. Midtvedt, J. Svensson, O. A. Nerushev, N. Lindvall, A. Isacsson, and E. E. B. Campbell, Nano Lett. **12**, 3526 (2012).

[19] N. N. Klimov, S. Jung, S. Zhu, T. Li, C. A. Wright, S. D. Solares, D. B. Newell, N. B. Zhitenev, and J. A. Stroscio, Science **336**, 1557 (2012).

[20] A. Georgi, P. Nemes-Incze, R. Carrillo-Bastos, D. Faria, S. V. Kusminskiy, D. W. Zhai, M. Schneider, D. Subramaniam, T. Mashoff, N. M. Freitag, M. Liebmann, M M. Pratzer, L. Wirtz, C. R. Woods, R. V. Gorbachev, Y. Cao, K. S. Novoselov, N. Sandler, and M. Morgenstern, Nano Lett. **17**, 2240 (2017).

[21] Y. Zhang, Y. Kim, M. J. Gilbert, and N. Mason, 2D Mater. **2**, 31 (2018).

[22] M. Goldsche, J. Sonntag, T. Khodkov, G. J. Verbiest, S. Reichardt, C. Neumann, T. Ouaj, N. von den Driesch, D. Buca, and C. Stampfer, Nano Lett. **18**, 1707 (2018).

[23] P. Jia, W. Chen, J. Qiao, M. Zhang, X. Zheng, Z. Xue, R. Liang, C. Tian, L. He, Z. Di, and X. Wang, Nat. Commun. **10**, 3127 (2019).

[24] Y. Jiang, M. Anelkovi, S. P. Milovanovi, L. Covaci, X. Lai, Y. Cao, K. Watanabe, T. Taniguchi, F. M. Peeters, A. K. Geim, and E. Y. Andrei, arXiv:1904.10147.

[25] M. Yamamoto, O. Pierre-Louis, J. Huang, M. S. Fuhrer, T. L. Einstein, and W. G. Cullen, Phys. Rev. X **2**, 041018 (2012).

[26] L. Tapasztó, T. Dumitrica, S. J. Kim, P. Nemes-Incze, C. Hwang, and L. P. Biró, Nat. Phys. **8**, 739 (2012).

[27] V. E. Calado, G. F. Schneider, A. M. M. G. Theulings, C. Dekker, and L. M. K. Vandersypen, Appl. Phys. Lett. **101**, 103116 (2012).

[28] S.-Y. Li, K.-K. Bai, L.-J. Yin, J.-B. Qiao, W.-X. Wang, and L. He, Phys. Rev. B **92**, 245302 (2015).

[29] S.-Y. Li, Y. Su, Y.-N. Ren, and L. He, arXiv:1812.04344.

[30] H. Lim, J. Jung, R. S. Ruoff, and Y. Kim, Nat. Commun. **6**, 8601 (2015).

[31] Y. H. Jiang, J. H. Mao, J. X. Duan, X. Y. Lai, K. Watanabe, T. Taniguchi, and E. Y. Andrei, Nano Lett. **17**, 2839 (2017).

[32] C. Ma, X. Sun, H. Du, J. Wang, M. Tian, A. Zhao, Y. Yamauchi, and B. Wang, Nano Lett. **18**, 6710 (2018).

[33] M. G. P. Carbone, A. C. Manikas, I. Souli, C. Pavlou, and C. Galioti, Nat. Commun. **10**, 1572 (2019).

[34] R. Banerjee, V.-H. Nguyen, T. Granzier-Nakajima, L. Pabbi, A. Lherbier, A. R. Binion, J.-C. Charlier, M. Terrones, and E. W. Hudson, Phys. Rev. B **100**, 115143 (2019).

[35] N. M. Freitag, L. A. Chizhova, P. Nemes-Incze, C. R. Woods, R. V. Gorbachev, Y. Cao, A. K. Geim, K. S. Novoselov, J. Burgdorfer, F. Libisch, and M. Morgenstern, Nano Lett. **16**, 5798 (2016).

[36] N. M. Freitag, T. Reisch, L. A. Chizhova, P. Nemes-Incze, C. Holl, C. R. Woods, R. V. Gorbachev, Y. Cao, A. K. Geim, K. S. Novoselov, J. Burgdorfer, F. Libisch, and M. Morgenstern, Nat. Nanotechnol. **13**, 392 (2018).

[37] D. Rainis, F. Taddei, M. Polini, G. Leon, F. Guinea, and V. I. Fal'ko, Phys. Rev. B **83**, 165403 (2011).

[38] Z. Qi, D. A. Bahamon, V. M. Pereira, H. S. Park, D. K. Campbell, and A. H. Castro Neto, Nano Lett. **13**, 2692 (2013).

[39] T. Low and F. Guinea, Nano Lett. **10**, 3551 (2010).

[40] M. Settnes, J. H. Garcia, and S. Roche, 2D Mater. **4**, 031006 (2017).

[41] B. Roy, Z.-X. Hu, and K. Yang, Phys. Rev. B **87**, 121408(R) (2013).

[42] T. Farajollahpour and A. Phirouznia, Sci. Rep. **7**, 17878 (2017).

[43] K.-J. Kim, Y. M. Blanter, and K.-H. Ahn, Phys. Rev B **84**, 081401(R) (2011).

[44] F. Zhai, X. Zhao, K. Chang, and H. Q. Xu, Phys. Rev. B **82**, 115442 (2010).

[45] T. Fujita, M. B. A. Jalil, and S. G. Tan, Appl. Phys. Lett. **97**, 043508 (2010).

[46] Z. Niu, J. Appl. Phys. **111**, 103712 (2012).

[47] Y. Song, F. Zhai, and Y. Guo, Appl. Phys. Lett. **103**, 183111 (2013).

[48] S. P. Milovanović and F. M. Peeters, Appl. Phys. Lett. **109**, 203108 (2016).

[49] V. Torres, P. Silva, E. A. T. de Souza, L. A. Silva, and D. A. Bahamon, Phys. Rev. B **100**, 205411 (2019).

[50] A. H. Castro Neto, F. Guinea, N. M. R. Peres, K. S. Novoselov, and A. K. Geim, Rev. Mod. Phys. **81**, 109 (2009).

[51] M. O. Goerbig, Rev. Mod. Phys. **83**, 1193 (2011).

[52] V. M. Pereira, A. H. Castro Neto, and N. M. R. Peres, Phys. Rev. B **80**, 045401 (2009).

[53] We have neglected the hopping modification that reflects p_z orbital rotations due to curvature (see Ref. [63]). We did not take this contribution into account because the maximum strain intensities considered in our studies are small ($\varepsilon_M < 2.1\%$) and deformations considered are extended in large areas compared to the atomic distances.

[54] E. Y. Andrei, G. Li, and X. Du, Rep. Prog. Phys. **75**, 056501 (2012).

[55] H. Suzuura and T. Ando, Phys. Rev. B **65**, 235412 (2002).

[56] F. Guinea, A. K. Geim, M. I. Katsnelson, and K. S. Novoselov, Phys. Rev. B **81**, 035408 (2010).

[57] J. V. Sloan, A. A. P. Sanjuan, Z. Wang, C. Horvath, and S. Barraza-Lopez, Phys. Rev. B **87**, 155436 (2013).

[58] S. Barraza-Lopez, A. A. P. Sanjuan, Z. Wang, and M. Vanević, Solid State Commun. **166**, 70 (2013).

[59] D. Midtvedt, C. H. Lewenkopf, and A. Croy, 2D Mater. **3**, 011005 (2016).

[60] See Supplemental Material at http://link.aps.org/supplemental/10.1103/PhysRevB.101.081410 for the derivation of asymp-

totic behavior for Landau level energy corrections and discussions about the scalar field effect.

[61] B. Amorim, A. Cortijo, F. de Juan, A. G. Grushine, F. Guinea, A. Gutiérrez-Rubio, H. Ochoa, V. Parente, R. Roldána, P. San-Jose, J. Schiefele, M. Sturla, and M. A. H. Vozmediano, Phys. Rep. **617**, 1 (2016).

[62] L. R. F. Lima, A. Dusko, and C. Lewenkopf, Phys. Rev. B **97**, 165405 (2018).

[63] E.-A. Kim and A. H. Castro Neto, Europhys. Lett. **84**, 57007 (2008).